INTERNATIONAL JOURNAL FOR NUMERICAL METHODS IN FLUIDS
Int. J. Numer. Meth. Fluids **28**: 815–840 (1998)

BOUNDARY ELEMENT ANALYSIS OF THREE-DIMENSIONAL MIXING FLOW OF NEWTONIAN AND VISCOELASTIC FLUIDS

R.E. KHAYAT[a,*], A. DERDOURI[b] AND D. FRAYCE[b]

[a] *Department of Mechanical and Materials Engineering, Faculty of Engineering Science, The University of Western Ontario, London, Ontario N6A 5B9, Canada*
[b] *National Research Council of Canada, Industrial Materials Institute, 75 de Mortagne Blvd., Boucherville, Quebec J4B 6Y4, Canada*

SUMMARY

The boundary element method (BEM) is implemented for the simulation of three-dimensional transient flows of typical relevance to mixing. Creeping Newtonian and viscoelastic fluids of the Maxwell type are examined. A boundary-only formulation in the time domain is proposed for linear viscoelastic flows. Special emphasis is placed on cavity flows involving simple- and multiple-connected moving domains. The BEM becomes particularly suited in multiple-connected flows, where part of the boundary (stirrer or rotor) is moving, and the remaining outer part (cavity or barrel) is at rest. In this case, conventional methods, such as the finite element method (FEM), generally require remeshing or mesh refinement of the three-dimensional fluid volume as the flow evolves and the domain of computation changes with time. The BEM is shown to be much easier to implement since the kinematics of the elements bounding the fluid is known (imposed). It is found that, for simple cavity flow induced by a rotating vane at constant angular velocity, the tractions at the vane tip and cavity face exhibit *non-linear* periodic dynamical behavior with time for fluids obeying *linear* constitutive equations. © 1998 John Wiley & Sons, Ltd.

KEY WORDS: boundary element method; three-dimensional mixing flow; Newtonian fluid; viscoelastic

1. INTRODUCTION

A wide range of flow problems in polymer processing involves the simultaneous presence of moving and fixed boundaries. The case of an extruder with the inner screw rotating and the outer barrel kept at rest, or that of mixing flow due to the motion (translation and/or rotation) of a stirrer inside a cavity, are typical applications. In addition to the presence of a moving boundary in such problems, the flow involved is unsteady. Typically, the flow becomes periodic after initial transients disappear following the early stages of the process. Periodic behavior results from the periodicity in geometry and the regularity in stirring motion. The time a flow takes to reach steady periodic motion can also be of practical interest, and may be strongly influenced by the viscoelastic character of the fluid. A wide range of Newtonian and viscoelastic flow problems must then be solved, where the entire domain of flow changes with time as a result of the movement of part of the boundary.

* Correspondence to: Department of Mechanical and Materials Engineering, Faculty of Engineering Science, The University of Western Ontario, London, Ontario N6A 5B9, Canada.

CCC 0271–2091/98/150815–26$17.50

Received 25 March 1997
Revised 9 October 1997

For moving boundary problems, the implementation of conventional numerical approaches, such as the methods of finite elements or finite difference, can often be extremely costly given the requirement for domain remeshing at each time step of the procedure, especially for complex three-dimensional flows. Certain classes of moving boundary problems can, however, be effectively treated by volume methods. For instance, in the case of the stirring rotor problem, a mesh may be affixed to the moving component, and another to the stationary component. The two meshes meet at an interface in the fluid (with or without grid overlap, depending on the type of interpolation used). In this case, the continuity of flow at the interface must be ensured. A solution is sought in each domain subject to boundary conditions at the moving wall and at the stationary wall. The two solutions are then matched at the interface. Although this matching approach can be suitable for moderately complex geometry, it may be difficult to implement in cases where the interface is moving or not simply shaped.

Remeshing or mesh refinement in three-dimensional flow are easily handled when the boundary element method (BEM) is used. The method does not require the matching at an interface in the domain interior, since the meshing is restricted to the boundary of the flow domain. The BEM offers this advantage when dealing with moving domain problems as it only necessitates the discretization of the boundary, and not that of the inner volume domain. The three-dimensional problem is therefore reduced to computing the flow field on the two-dimensional boundary. Consider the flow inside a cavity induced by the movement of a stirrer; only the (inner) cavity walls together with the (outer) surface of the stirrer need to be discretized.

Modeling of the mixing process has been extensively studied in the transition or turbulent regime [1–4], but less so for the laminar regime, especially of viscoelastic fluids. Chien *et al.* [5] proposed a versatile experimental set-up to generate various low-Reynolds number situations in closed long cavities and to visualize streamlines. In that study, the essentially planar flow was examined together with the deviation of the velocity component in the direction perpendicular to the plane of the flow. Comparison between photographs taken under different flow conditions, and numerical prediction of FEM results, led to excellent agreement. Efficiency of the mixing process was also assessed according to the dimensionless frequency of oscillation for each flow configuration. Alternate periodic flows were found more efficient from a mixing standpoint than from steady flows since they are not always integrable and may lead to the presence of a Smale horseshoe function [6] and chaotic behavior. More recently, Leong and Ottino [7] studied the macroscopic structures of chaotic mixing. Experimental stretching rate was taken as a mixing criterion for several conditions of flow bifurcation, birth and collapse of islands. The lid-driven rectangular shaped cavity flow problem was investigated by Cortes and Miller [8]. Simulations were carried out using the spectral method for two- and three-dimensional flows for the Laplace and Navier–Stokes equations with pressure correction at Reynolds numbers up to 10 000. The algorithm was quite efficient, requiring very modest computing resources for the type of problem investigated.

Mixing of polymer blends was simulated by Graman *et al.* [9] using the BEM for two-dimensional non-Newtonian flow and advective heat transfer. The convective non-linearities in the energy equation and non-linearities related to the non-Newtonian nature of the flow were treated using the dual reciprocity BEM, a method proved to be numerically stable. The dynamics of vortex formation in cavity flow were studied by Gustafson and Halasi [10] for a wide range of Reynolds numbers (from 10^{-6} to 2000), and various aspect ratios. These authors computed unsteady two-dimensional solutions using the finite difference (control volume) method with Euler explicit time stepping. Velocity distributions, pressure gradients as well as the kinetic energy, eddy centers, secondary eddy separations and coalescence were computed and validated against earlier data. Bruneau and Jouron [11] numerically predicted

the formation of vortex flow in two-dimensional cavities at higher Reynolds numbers (100–5000), and described the limit conditions for the onset of turbulence. Various numerical techniques were used, consisting of the finite difference method with staggered grids for the treatment of the convection terms in the Navier–Stokes equations and relaxation for all the variables. For higher Reynolds numbers, transition to turbulence and bifurcation phenomena in a two-dimensional cavity, refer to the works of Goodrich *et al.* [12] and Jie Shen [13] for further details.

The present paper is part of a series of studies on the implementation of the BEM and the application of the method to problems in materials processing. Such problems include: (1) The two- and three-dimensional flows in gas-assisted injection moulding, where the fluid is confined between the melt front (free-surface) and the gas/melt interface [14]. The aim of the simulation was to predict the amount of melt deposited along the cavity walls as the gas penetrates the melt. (2) The three-dimensional transient heat conduction in complex parts [15]. The dual reciprocity method was used to transform the volume integral arising from the transient term into a boundary integral. (3) The flow of metal in the shot sleeve of die casting machines [16]. The flow is induced by the movement of a plunger. An Eulerian–Lagrangian approach was used to compute the evolution of the three-dimensional surface. (4) The planar deformation of drops in confined flow [17], with particular emphasis on the influence of shear and elongation in a convergent/divergent channel.

The present study explores the applicability of the BEM in areas of polymer processing where conventional methods such as the FEM face a big challenge in implementation. In particular, the potential of the BEM is demonstrated as it is applied to a wide range of moving boundary problems. Particular emphasis is placed on the mixing of Newtonian and viscoelastic fluids. Only linear viscoelastic fluids of the Maxwell-type [48] are considered, and the analysis is thus limited to flows with small rates of strain.

For non-linear viscoelastic problems, the BEM traditionally requires the discretization of a volume integral, which includes all the non-linear terms in the form of a pseudo-body force [18,19,45,46]. In this case, the major advantage of the BEM is lost as a result of the inner volume discretization. More recent techniques, such as the methods of dual- and multiple-reciprocity have been developed to transform the volume integral into a boundary integral. Although these methods still require the evaluation of the flow field at internal points, they do not require the discretization of the inner domain, and the BEM retains its major advantage. However, the capability of such techniques to handle highly non-linear problems, such as flows with strong inertia or (elastic) normal stress effects, remains questionable [20–22]. The present work will thus be limited to linear viscoelastic flow obeying Maxwell's equation.

Unlike many existing BEM formulations for linear viscoelastic problems in the frequency domain [23–25], the boundary integral equations in the current study are derived and solved in the time domain. The derivation of the boundary integral equation for viscoelastic flow is based on the Laplace transform of the flow variables. The association of the integral transform of the viscoelastic solution with that associated with the Newtonian flow problem is similar to the correspondence principle for linear viscoelastic solids or the elastico–viscoelastic analogy [25–27]. Although the derivation given here uses the Laplace transform, an analogous procedure follows from the use of the Fourier transform. Read [28] was the first to recognize this association through the Fourier transform, while Sips [29], Brull [30] and Lee [31] gave the corresponding Laplace transform results. The present procedure involves replacing the viscosity by the appropriate form in the transformed equations, and reinterpreting the transformed flow variables as transformed viscoelastic field variables. The transformed equations are then solved and the solution is inverted to obtain the evolution of the flow field with time. In the

present work, however, the inversion is avoided and the boundary integral equations are derived in the time domain. A time marching scheme is then implemented for the discretization of the time derivatives and the solution of the integral equations.

The paper is organized as follows. The governing equations, boundary and initial conditions are discussed in Section 2. The boundary integral equations for viscoelastic and Newtonian flows are derived in Section 3. Numerical results are given in Section 4, where calculations are carried out first for simple steady cavity flow of a Newtonian fluid, thus allowing comparisons with experiments and results based on the FEM. The validity of the method is further assessed by examining the rate of convergence and CPU requirement for each method. The validity of the viscoelastic formulation is assessed against the analytical solution for transient Taylor–Couette flow. Unsteady cavity flows involving multiple-connected domains are then examined for the cases of oscillatory and rotating mixing processes. Discussion and concluding remarks are given in Section 5.

2. GOVERNING EQUATIONS AND BOUNDARY CONDITIONS

In this section, the governing equations and boundary conditions are briefly reviewed, together with some of the assumptions adopted in the present study. Consider a fluid occupying a three-dimensional region, $\Omega(t)$, that may change with time, t. Let $\Gamma(t) = \Gamma_s \cup \Gamma_m(t)$ be the surrounding boundary of $\Omega(t)$, with Γ_s being stationary and $\Gamma_m(t)$ undergoing rigid-body motion such as translation (oscillation) and/or rotation. The flow is thus induced by the movement of $\Gamma_m(t)$ and/or by the imposed velocity or traction on Γ_s.

The fluid is assumed to be an incompressible Newtonian or viscoelastic fluid. Inertia and body forces are assumed negligible. The conservation of mass and linear momentum equations are then given by

$$\nabla \cdot \mathbf{u}(\mathbf{x}, t) = 0, \qquad \nabla \cdot \sigma(\mathbf{x}, t) = 0, \qquad \mathbf{x} \in \Omega(t) \cup \Gamma(t), \tag{1}$$

where ∇ is the gradient operator, $\mathbf{x}$ is the position vector, $\mathbf{u}(\mathbf{x}, t)$ is the velocity vector and $\sigma(\mathbf{x}, t)$ is the total stress tensor given in terms of the hydrostatic pressure $p(\mathbf{x}, t)$ and excess stress tensor $\tau(\mathbf{x}, t)$, such that $\sigma(\mathbf{x}, t) = -p(\mathbf{x}, t)\mathbf{I} + \tau(\mathbf{x}, t)$, where $\mathbf{I}$ is the unit tensor. In the present study, the fluid is assumed to obey the linear viscoelastic constitutive equation of the Maxwell type, so that

$$\lambda \frac{\partial \tau(\mathbf{x}, t)}{\partial t} + \tau(\mathbf{x}, t) = \mu[\nabla \mathbf{u}(\mathbf{x}, t)] + \nabla \mathbf{u}^t(\mathbf{x}, t), \quad \mathbf{x} \in \Omega(t) \cup \Gamma(t), \tag{2}$$

where λ is the relaxation time and μ is the viscosity of the fluid. The acceleration term $\partial \mathbf{u}/\partial t$ in the momentum conservation equation is neglected, so that for a Newtonian fluid, the formulation in question is not strictly unsteady, but quasi-steady. This quasi-steady state assumption is valid whenever $L^2/\nu \ll T$, where L and T are typical characteristic length and time of the flow, respectively, and $\nu = \mu/\rho$ is the kinematic viscosity (ρ being the density). In the present case, $T \approx L/U$, where U is a typical value of the driving velocity. Thus, for the quasi-steady state assumption to apply, one must have $UL/\nu \ll 1$. This is typically the case for fluids of interest to mixing problems. Note also that this inequality is implied by the smallness of the Reynolds number. Physically, the quasi-steady state approximation means that a Newtonian fluid immediately adjusts to changes in the movement of the boundary or boundary conditions. This is not necessarily the case for a viscoelastic fluid.

The system (1)–(2) must be supplemented with appropriate boundary and initial conditions, which depend on the flow configuration examined. Typically, however, the velocity is prescribed on part of the boundary, and the velocity or the traction is imposed on the remaining part. In the present work, the velocity is always prescribed on $\Gamma_m(t)$, so that

$$\mathbf{u}(\mathbf{x}, t) = \mathbf{u}_m(t), \quad \mathbf{x} \in \Gamma_m(t), \tag{3a}$$

and either the velocity or the traction is imposed on the stationary part

$$\mathbf{u}(\mathbf{x}, t) = \mathbf{u}_s(t) \quad \text{or} \quad \mathbf{t}(\mathbf{x}, t) = \mathbf{t}_s(t), \quad \mathbf{x} \in \Gamma_s, \tag{3b}$$

where the traction is defined as $\mathbf{t}(\mathbf{x}, t) \equiv \sigma(\mathbf{x}, t) \cdot \mathbf{n}(\mathbf{x}, t)$, $\mathbf{n}(\mathbf{x}, t)$ being the unit normal vector at the boundary. As to the initial conditions, the fluid is assumed to be initially at rest; the fluid is in a stress free state

$$\mathbf{u}(\mathbf{x}, t = 0) \equiv 0, \qquad \mathbf{t}(\mathbf{x}, t = 0) = 0, \quad \mathbf{x} \in \Omega(t = 0) \cup \Gamma(t = 0). \tag{4}$$

The assumption of initial equilibrium may seem incompatible with the assumption that the acceleration term in the momentum equation is negligible. This is certainly true if the initial jump in the boundary condition(s) is significant. However, since the viscosity of the fluid and the imposed velocity are typically low, the assumption of negligible acceleration, even initially, may still be valid. Condition (4) greatly simplifies the solution procedure for the viscoelastic flow as will be seen below.

3. BOUNDARY INTEGRAL FORMULATION AND NUMERICAL IMPLEMENTATION

In this section, the boundary integral equation is derived for the general viscoelastic flow problem, and its numerical implementation is carried out in the context of mixing flow. The numerical solution procedure and time marching scheme are also described. While the formalism behind the BEM for Stokes flow is well established [32,33], that corresponding to viscoelastic fluids is relatively unexplored. Given the linearity of the constitutive equation (2), the problem reduces to that corresponding to Stokes flow in the frequency domain upon Laplace transformation of the governing equations. The so-called Voltera principle in the frequency domain, which is also known as the correspondence principle [25–27], allows the solution of a boundary value problem in viscoelasticity to be obtained from the solution of the corresponding Newtonian problem, with the viscosity being replaced by a transformed characteristic of the fluid. The final boundary integral equations and their solutions are obtained in the time domain.

3.1. Boundary integral equations

The first step in the procedure consists of taking the Laplace transform of the governing equations, so that the transformed continuity and momentum equations (1) are given by

$$\nabla \cdot \bar{\mathbf{u}}(\mathbf{x}, s) = 0, \qquad \nabla \bar{p}(\mathbf{x}, s) - \nabla \cdot \bar{\tau}(\mathbf{x}, s) = 0, \tag{5}$$

where a bar over the velocity and stress variables denotes Laplace transformation. An expression for the transformed excess stress is also obtained from Equation (2) in terms of the transformed rate of strain tensor, which is mathematically equivalent to Newton's law of viscosity

$$\bar{\tau}(\mathbf{x}, s) = \bar{\mu}[\nabla\bar{\mathbf{u}}(\mathbf{x}, s) + \nabla\bar{\mathbf{u}}^{t}(\mathbf{x}, s)], \quad \bar{\mu} = \frac{\mu}{\lambda s + 1}. \tag{6}$$

Note that an equivalent viscosity is now obtained that is a function of the Laplace parameter s. The problem is now solved similarly to the flow of a Newtonian fluid in the frequency domain. In order to derive the integral representation for Equations (5) and (6), the fundamental solution for the problem is needed. For a Newtonian fluid, this singular solution corresponds to the velocity and stress fields at a point $\mathbf{x}$ produced by a point force $\bar{\mathbf{F}}(s)\delta(\mathbf{x}-\mathbf{y})$ located at $\mathbf{y}$. In this case, the acting force is generally a function of the parameter s, and therefore depends on time. For a viscoelastic fluid, this also corresponds to the same force that starts to act initially at time $t = 0$. In other words, the force in real time is given by $\mathbf{F}\delta(\mathbf{x}-\mathbf{y})H(t)$, where δ is the Dirac delta function and H is the Heavyside function. Denoting the singular solution variables with an asterisk, and taking the Laplace transform of the viscoelastic equations over the infinite medium, the problem reduces to that corresponding to Stokes flow in the frequency domain

$$\nabla\cdot\bar{\mathbf{u}}^{*}(\mathbf{x} \mid \mathbf{y}, s) = 0, \qquad \nabla\bar{p}^{*}(\mathbf{x} \mid \mathbf{y}, s) - \nabla\cdot\bar{\tau}^{*}(\mathbf{x} \mid \mathbf{y}, s) = \bar{\mathbf{F}}(s)\,\delta(\mathbf{x}-\mathbf{y}), \tag{7a}$$

with the following boundary conditions

$$|\bar{\mathbf{u}}^{*}(\mathbf{x} \mid \mathbf{y}, s)| \to 0, \qquad |\bar{\tau}^{*}(\mathbf{x} \mid \mathbf{y}, s)| \to 0, \quad \text{as} \quad |\mathbf{x}| \to \infty. \tag{7b}$$

This yields the following expressions for the transformed velocity $\bar{\mathbf{u}}^{*}(\mathbf{x} \mid \mathbf{y}, s)$ and stress $\bar{\sigma}^{*}(\mathbf{x} \mid \mathbf{y}, s) = -\bar{p}^{*}(\mathbf{x} \mid \mathbf{y}, s)\mathbf{I} + \bar{\tau}^{*}(\mathbf{x} \mid \mathbf{y}, s)$, namely,

$$\bar{\mathbf{u}}^{*}(\mathbf{x} \mid \mathbf{y}, s) = (\lambda s + 1)\mathbf{J}(\mathbf{x} \mid \mathbf{y})\cdot\bar{\mathbf{F}}(s) \qquad \bar{\sigma}^{*}(\mathbf{x} \mid \mathbf{y}, s) = \mathbf{K}(\mathbf{x} \mid \mathbf{y})\cdot\bar{\mathbf{F}}(s), \tag{8}$$

where the expression for $\bar{\mu}$ from (6) has been used. The kernels, or Green's functions, $\mathbf{J}$ and $\mathbf{K}$ are second and third rank tensors, respectively, and are given by

$$\mathbf{J}(\mathbf{x} \mid \mathbf{y}) = \frac{1}{8\pi\mu}\left(\frac{\mathbf{I}}{t} + \frac{\mathbf{rr}}{r^{3}}\right), \qquad \mathbf{K}(\mathbf{x} \mid \mathbf{y}) = \frac{3}{4\pi}\frac{\mathbf{rrr}}{r^{5}}, \tag{9}$$

for an unbounded three-dimensional domain. Here $\mathbf{r} = \mathbf{x} - \mathbf{y}$ and $r = |\mathbf{r}|$. Note that $\mathbf{J}$ and $\mathbf{K}$ are, respectively, symmetric and anti-symmetric tensors with respect to $\mathbf{r}$. The corresponding integral representation is now derived similar to that corresponding to Stokes flow. The Reciprocal (Green's) theorem is first invoked, relating the fields $(\bar{\mathbf{u}}, \bar{\sigma})$ and $(\bar{\mathbf{u}}^{*}, \bar{\sigma}^{*})$. The theorem is straightforward to derive [32], and its statement for the present problem is as follows

$$\int_{\Omega} \{\bar{\mathbf{u}}(\mathbf{y}, s)\cdot[\nabla_{\mathbf{y}}\cdot\bar{\sigma}^{*}(\mathbf{x} \mid \mathbf{y}, s)] - \bar{\mathbf{u}}^{*}(\mathbf{x} \mid \mathbf{y}, s)\cdot[\nabla_{\mathbf{y}}\cdot\bar{\sigma}(\mathbf{y}, s)]\}\,\mathrm{d}\Omega_{\mathbf{y}}$$
$$= \int_{\Gamma} \mathbf{n}(\mathbf{y})\cdot[\bar{\sigma}^{*}(\mathbf{x} \mid \mathbf{y}, s)\cdot\bar{\mathbf{u}}(\mathbf{y}, s) - \bar{\sigma}(\mathbf{y}, \mathrm{s})\cdot\bar{\mathbf{u}}^{*}(\mathbf{x} \mid \mathbf{y}, s)]\,\mathrm{d}\Gamma_{\mathbf{y}}, \tag{10}$$

where s is just a parameter. Substitution of the fundamental singular solution (8) into the theorem (10), using (1), removing the arbitrary vector $\bar{\mathbf{F}}$, and interchanging the labels $\mathbf{x}$ and $\mathbf{y}$, lead to the following integral equation in the frequency domain

$$\int_{\Gamma} \mathbf{n}(\mathbf{y})\cdot[(\lambda s + 1)\bar{\sigma}(\mathbf{y}, s)\cdot\mathbf{J}(\mathbf{x} \mid \mathbf{y})]\,\mathrm{d}\Gamma_{\mathbf{y}} - \int_{\Gamma} \mathbf{n}(\mathbf{y})\cdot[\bar{\mathbf{u}}(\mathbf{y}, s)\cdot\mathbf{K}(\mathbf{x} \mid \mathbf{y})]\,\mathrm{d}\Gamma_{\mathbf{y}}$$
$$= c(\mathbf{x})\bar{\mathbf{u}}(\mathbf{x}, s), \quad \mathbf{x} \in \Omega \cup \Gamma, \tag{11}$$

where $c(\mathbf{x})$ is equal to 1 for $\mathbf{x}$ belonging to the inside of Ω, and for a point on the boundary Γ, its value depends on the jump in the value of the first integral on the boundary as the boundary is crossed. Thus $c = 1/2$ if the boundary is Lyapunov-smooth; which requires that a local tangent to the boundary exists everywhere. This assumption, however, is not valid in the vicinity of sharp corners, cusps or edges. In such cases, a separate treatment is needed. This issue will be further discussed when the numerical implementation is covered (see also Reference [34]).

The inverse Laplace transform of Equation (11) is taken to obtain the desired integral equation in the time domain. It is not difficult to see that the Laplace inversion of Equation (11) leads to the following time dependent integral equation

$$\int_{\Gamma(t)} \mathbf{n}(\mathbf{y}, t) \cdot \left[\lambda \frac{\partial \sigma(\mathbf{y}, t)}{\partial t} + \sigma(\mathbf{y}, t) \right] \cdot \mathbf{J}(\mathbf{x} \mid \mathbf{y}) \, d\Gamma_{\mathbf{y}} - \int_{\Gamma(t)} \mathbf{n}(\mathbf{y}, t) \cdot \mathbf{u}(\mathbf{y}, \mathrm{t}) \cdot \mathbf{K}(\mathbf{x} \mid \mathbf{y}) \, d\Gamma_{\mathbf{y}}$$
$$= c(\mathbf{x}, t)\mathbf{u}(\mathbf{x}, t), \quad \mathbf{x} \in \Gamma(t), \tag{12}$$

for the class of problems envisaged in the present study. Recall that $\Gamma(t) = \Gamma_s \cup \Gamma_m(t)$, which represents the surface bounding the volume $\Omega(t)$ occupied by the fluid. In the derivation of Equation (12), the fluid is tacitly assumed to be initially in a state of rest, or, more particularly, in a stress free state. As mentioned earlier, this assumption greatly simplifies the formulation. Indeed, the inclusion of an initial stress condition leads to an additional term in Equation (6) when the Laplace transform of the constitutive equation (2) is taken. If the initial stress is not generally a constant, thus is dependent on position, a volume integral emerges and must be added to the integral equation (11) in the frequency domain. Correspondingly, a volume integral emerges in Equation (12) in the time domain. It is obvious that the presence of a volume integral complicates matters significantly, and may not be necessary for a wide range of practical flow problems.

In the limit of a Newtonian fluid ($\lambda = 0$), one recovers the familiar integral equation corresponding to Stokes flow

$$\int_{\Gamma(t)} \mathbf{t}(\mathbf{y}, t) \cdot \mathbf{J}(\mathbf{x} \mid \mathbf{y}) \, d\Gamma_{\mathbf{y}} - \int_{\Gamma(t)} \mathbf{n}(\mathbf{y}, t) \cdot \mathbf{u}(\mathbf{y}, t) \cdot \mathbf{K}(\mathbf{x} \mid \mathbf{y}) \, d\Gamma_{\mathbf{y}} = c(\mathbf{x}, t)\mathbf{u}(\mathbf{x}, t), \quad \mathbf{x} \in \Gamma(t), \tag{13}$$

where the traction $\mathbf{t}(\mathbf{x}, t) = \sigma(\mathbf{x}, t) \cdot \mathbf{n}(\mathbf{x}, t)$ is introduced. Unlike Equation (12), Equation (13) relates directly the velocity field, $\mathbf{u}(\mathbf{x}, t)$, at any point inside the fluid region, $\Omega(t)$, or on the boundary, $\Gamma(t)$, to the traction, $\mathbf{t}(\mathbf{x}, t)$. The situation is quite different for the viscoelastic flow problem.

Equation (12) is valid for the general transient viscoelastic flow with moving boundary, and the normal to the boundary changing with time. A direct relationship between velocity and traction is not possible unless the normal vector is constant with time. This corresponds to the situation when the domain occupied by the fluid, Ω_s, and the surrounding boundary, Γ_s, are both stationary. In this case, Equation (12) reduces to

$$\int_{\Gamma_s} \left[\lambda \frac{\partial \mathbf{t}(\mathbf{y}, t)}{\partial t} + \mathbf{t}(\mathbf{y}, t) \right] \cdot \mathbf{J}(\mathbf{x} \mid \mathbf{y}) \, d\Gamma_{\mathbf{y}} - \int_{\Gamma_s} \mathbf{n}(\mathbf{y}) \cdot \mathbf{u}(\mathbf{y}, t) \cdot \mathbf{K}(\mathbf{x} \mid \mathbf{y}) \, d\Gamma_{\mathbf{y}} = c(\mathbf{x})\mathbf{u}(\mathbf{x}, t), \quad \mathbf{x} \in \Gamma_s. \tag{14}$$

Obviously, even if Γ_s is stationary, the (unknown or imposed) traction and velocity may vary with time. Note that c does not depend on time in this case. In the present study, problems with the domain of the fluid changing with time are of particular interest, typically as in mixing processes. A solution is thus sought to the time-dependent Equation (12).

3.2. Numerical implementation and time marching scheme

The solution of Equation (12) is first obtained for the general moving boundary problem and then implemented to mixing. If the time derivative is approximated by finite difference, and higher-order terms are neglected, Equation (12) can be reduced to an integral equation similar to that corresponding to Stokes flow with a source term on the boundary. Using an Euler scheme, the stress terms in Equation (12) reduce to

$$\lambda \frac{\partial \sigma(\mathbf{y}, t)}{\partial t} + \sigma(\mathbf{y}, t) \approx \left(\frac{\lambda}{\Delta t} + 1\right)\sigma(\mathbf{y}, t) - \frac{\lambda}{\Delta t}\sigma(\mathbf{y}, t - \Delta t) + O(\Delta t), \tag{15}$$

where terms of $O(\Delta t)$ are neglected. In this case, Equation (12) reduces to an integral relationship between the velocity and traction at the current time and the stress at the previous time steps

$$c(\mathbf{x}, t)\mathbf{u}(\mathbf{x}, t) + \int_{\Gamma(t)} \mathbf{n}(\mathbf{y}, t)\cdot\mathbf{u}(\mathbf{y}, t)\cdot\mathbf{K}(\mathbf{x} \mid \mathbf{y})\, d\Gamma_{\mathbf{y}} - \left(\frac{\lambda}{\Delta t} + 1\right)\int_{\Gamma(t)} \mathbf{t}(\mathbf{y}, t)\cdot\mathbf{J}(\mathbf{x} \mid \mathbf{y})\, d\Gamma_{\mathbf{y}}$$
$$= \frac{\lambda}{\Delta t}\int_{\Gamma(t)} \mathbf{n}(\mathbf{y}, t)\cdot\sigma(\mathbf{y}, t - \Delta t)\cdot\mathbf{J}(\mathbf{x} \mid \mathbf{y})\, d\Gamma_{\mathbf{y}}, \quad \mathbf{x}\in\Gamma(t). \tag{16}$$

Thus, if the flow field is known at the previous step, $t - \Delta t$, the previous stress components can be determined and used in the evaluation of the integral on the right-hand side. A further approximation may be used, which greatly simplifies the numerical computation if the normal vector at time t is expanded around the previous time step. If only the leading term in the Taylor expansion of the normal vector is kept, such that $\mathbf{n}(\mathbf{y}, t) \approx \mathbf{n}(\mathbf{y}, t - \Delta t) + O(\Delta t)$, then Equation (16) reduces to

$$c(\mathbf{x}, t)\mathbf{u}(\mathbf{x}, \mathbf{t}) + \int_{\Gamma(t)} \mathbf{n}(\mathbf{y}, t)\cdot\mathbf{u}(\mathbf{y}, t)\cdot\mathbf{K}(\mathbf{x} \mid \mathbf{y})\, d\Gamma_{\mathbf{y}} - \left(\frac{\lambda}{\Delta t} + 1\right)\int_{\Gamma(t)} \mathbf{t}(\mathbf{y}, t)\cdot\mathbf{J}(\mathbf{x} \mid \mathbf{y})\, d\Gamma_{\mathbf{y}}$$
$$= \frac{\lambda}{\Delta t}\int_{\Gamma(t)} \mathbf{t}(\mathbf{y}, t - \Delta t)\cdot\mathbf{J}(\mathbf{x} \mid \mathbf{y})\, d\Gamma_{\mathbf{y}}, \quad \mathbf{x}\in\Gamma(t). \tag{17}$$

Equation (17) is much easier to handle than Equation (16) since the source integral includes the traction and not the stress. Similarly to Stokes flow, if the velocity is specified everywhere on $\Gamma(t)$, then Equation (17) is a Fredholm equation of the *first kind* for the traction $\mathbf{t}$, and of the *second kind* for the velocity $\mathbf{u}$, if the traction is specified everywhere on the boundary.

The current formulation and its computer implementation are intended for typical mixing problems. The geometry involved is usually complex and three-dimensional. Typically, a mixing process involves the motion of part of the boundary, such as in lid-driven cavity flow, or the presence of a second moving boundary, such as a rotor or a stirrer. It is obvious that the BEM becomes particularly advantageous over domain methods in the presence of a moving obstacle because the computational domain evolves with time. A conventional domain method, such as the FEM, generally necessitates a continuous remeshing of the inner domain; e.g. the volume domain located between the rotor and the housing needs remeshing, although for some problems the volume meshing can be constant as mentioned in Section 1. The BEM requires the discretization of the rigid boundaries only. The discretization of the moving boundary (rotor) does not pose any difficulty. The kinematics of each of the discretization elements is known (imposed) given the boundary is undergoing rigid-body motion. In the present work, the motion of the moving boundary is always known so that the velocity will be

prescribed on $\Gamma_m(t)$. In this case, Equation (17) reduces to the following integral equation for a point on the stationary boundary

$$c(\mathbf{x}, t)\,\mathbf{u}(\mathbf{x}, t) + \int_{\Gamma_S} \mathbf{u}(\mathbf{y}, t)\cdot[\mathbf{n}(\mathbf{y}, t)\cdot\mathbf{K}(\mathbf{x}\mid\mathbf{y})]\,d\Gamma_y - \left(\frac{\lambda}{\Delta t}+1\right)\int_{\Gamma_s\cup\Gamma_m(t)} \mathbf{t}(\mathbf{y}, t)\cdot\mathbf{J}(\mathbf{x}\mid\mathbf{y})\,d\Gamma_y$$
$$= \frac{\lambda}{\Delta t}\int_{\Gamma_s\cup\Gamma_m(t)} \mathbf{t}(\mathbf{y}, t-\Delta t)\cdot\mathbf{J}(\mathbf{x}\mid\mathbf{y})\,d\Gamma_y - \int_{\Gamma_m(t)} \mathbf{u}_m(\mathbf{y}, t)\cdot[\mathbf{n}(\mathbf{y}, t)\cdot\mathbf{K}(\mathbf{x}\mid\mathbf{y})]\,d\Gamma_y, \quad \mathbf{x}\in\Gamma_s. \tag{18}$$

where $\mathbf{u}_m$ is the velocity imposed on $\Gamma_m(t)$. The unknowns in this case being the traction on $\Gamma_m(t)$, and the traction and velocity on Γ_s. Note that not all velocity components are necessarily known on Γ_s; there may be symmetry or slip conditions at the boundary. For a point on the moving boundary, Equation (17) leads to

$$\int_{\Gamma_s} \mathbf{n}(\mathbf{y}, t)\cdot\mathbf{u}(\mathbf{y}, t)\cdot\mathbf{K}(\mathbf{x}\mid\mathbf{y})\,d\Gamma_y - \left(\frac{\lambda}{\Delta t}+1\right)\int_{\Gamma_s\cup\Gamma_m(t)} \mathbf{t}(\mathbf{y}, t)\cdot\mathbf{J}(\mathbf{x}\mid\mathbf{y})\,d\Gamma_y$$
$$= \frac{\lambda}{\Delta t}\int_{\Gamma_s\cup\Gamma_m(t)} \mathbf{t}(\mathbf{y}, t-\Delta t)\cdot\mathbf{J}(\mathbf{x}\mid\mathbf{y})\,d\Gamma_y - \int_{\Gamma_m(t)} \mathbf{u}_m(\mathbf{y}, t)\cdot\mathbf{K}(\mathbf{x}\mid\mathbf{y})\,d\Gamma_y$$
$$- c(\mathbf{x}, t)\mathbf{u}_m(\mathbf{x}, t), \quad \mathbf{x}\in\Gamma_m(t). \tag{19}$$

Consider the evaluation of $c(\mathbf{x}, t)$ for $\mathbf{x}$ belonging to $\Gamma(t) = \Gamma_s\cup\Gamma_m(t)$. At each time step, t, the value of $c(\mathbf{x}, t)$ depends solely on the geometry of the boundary involved. Thus $c(\mathbf{x}, t) = 1/2$ for a smooth boundary. More generally, if a uniform velocity field, such as $\mathbf{u}(\mathbf{x}, t) = u\mathbf{e}$, is applied over the boundary (assuming a closed cavity), $\mathbf{e}$ being the direction of the velocity and u its magnitude, then all derivatives (including tractions and stresses) must vanish. Hence, at any time t, Equation (16) reduces to

$$c(\mathbf{x}, t) = \int_{\Gamma(t)} [\mathbf{n}(\mathbf{y}, t)\cdot\mathbf{K}(\mathbf{x}\mid\mathbf{y})]\cdot:\mathbf{ee}\,d\Gamma_y, \quad \mathbf{x}\in\Gamma(t). \tag{20}$$

Equations (18) and (19) may be solved using constant or higher-order elements. In this study, the simplest form of the BEM is adopted, and the boundary is discretized into a finite number of constant triangular elements. The velocity and traction are thus assumed to be constant over each surface element and equal to the values at the centroid. In this case, since there are no corner nodes on which the unknown variables are evaluated, the value of $c(\mathbf{x}, t) = 1/2$. The resulting discretized equations represent a set of linear algebraic equations in the velocity and traction at the boundary once the integrals are evaluated over each element. The evaluation of the integrals is carried out numerically using Gauss quadrature formulae in the absence of singularities. Since the kernels $\mathbf{J}$ and $\mathbf{K}$ have integrable singularity at $\mathbf{x} = \mathbf{y}$, some care must be taken in the numerical evaluation of the singular integrals. Common procedures either cut out a region surrounding the singularity and perform the integration analytically [35], or subtract the singularity directly in the numerical approximation of the integral [36]. In the case of constant elements, the analytical evaluation of the singular integrals is straightforward in two-dimensions. For the present three-dimensional flow, the singular integrals can also be evaluated analytically through the Cauchy Principle Value theorem [37]. The resulting system of linear equations is solved using the LU factorization method.

4. NUMERICAL ASSESSMENT AND RESULTS

In this section, the solutions of Equations (18) and (19) are presented for steady and transient three-dimensional flows of Newtonian and viscoelastic fluids. The accuracy of the code is

assessed against finite element and analytical solutions. Comparison with experiments is also carried out for steady simple lid-driven cavity flow of a Newtonian fluid. Transient effects are examined for oscillatory and rotating flows. These flows involve the translation and rotation of three-dimensional objects moving inside rectangular shape cavities typically as in mixing.

4.1. Assessment of convergence and accuracy for Newtonian fluids

The accuracy and CPU requirement of the method are assessed by comparing results based on the BEM with those based on the FEM using the commercial code POLYFLOW™. This comparison is limited to Newtonian fluids. All computations are carried out on an IBM (RISK) 590 machine with a speed of 130 MFLOPS (Linpack). The swapping in this case is minimal or non-existent. The computation domain corresponds to a cubic cavity of unit side length, given by $(x, y, z) \in [0, 1]$. The face $y = 1$ is assumed to move at a velocity $(1, 0, 0)$. All dimensions are relative. Stick conditions are imposed on all faces except at the side $z = 1$, which is assumed to be lubricated (or a plane of symmetry). On this side, the velocity distributions based on the BEM and the FEM are compared. In this case, the three velocity components (u_x, u_y, u_z) vanish on all faces except at the face $z = 1$, where $u_z = 0$ and $t_x = t_y = 0$.

The u_x and u_y velocity contours in the lubricated (symmetry) plane $z = 1$, and a typical boundary element mesh used in the calculation, are shown in Figure 1. It is clear from Figure 1(a) and (b), that most flow activity is concentrated around the edges of the cubic cavity. Note also the symmetry of the flow field with respect to the plane $x = 0.5$ (see also the comparison with the experiment below). Three FEM mesh sizes are used, corresponding to a total number of internal and external nodes $N = 64$, 216 and 729, and five BEM meshes also corresponding to a total number of internal and external nodes $N \in [216, 1134]$. Note that the internal nodes in the case of the BEM are not used in the computation but are mentioned here for clarity. In fact, the comparison is meaningful only if the total number of nodes for both methods is comparable. It is understood that although the number of degrees of freedom, corresponding to a given mesh size, can be relatively much smaller for the BEM than for the FEM, the resulting discretized algebraic system is full in the former case and sparse in the latter. Thus, it is difficult *a priori* to anticipate which of the two methods is more advantageous regarding space and time requirement.

The u_x velocity distributions, which are based on various mesh sizes for the FEM and BEM, are shown in Figure 2. The figure indicates that convergence for the FEM is reasonably achieved between the second and third curves, and that the FEM results are accurate only for the finest mesh ($N = 729$) used when compared with the BEM results. The calculation based on a finer FEM mesh was also attempted, but storage problems were encountered. Calculations based on the BEM indicate that convergence is relatively faster. The three finest BEM meshes ($N = 720$, 990 and 1134) lead essentially to the same results, and may then be regarded as the exact solution to the problem. This convergence is also confirmed from the trend based on the FEM curves. Comparison between the FEM with $N = 729$ and the BEM with $N = 720$ tends to confirm the general observation that the BEM is more accurate than the FEM since the solution has already converged in this case. This observation is usually well established for two-dimensional problems.

The (absolute) CPU required for each case and method studied was also monitored. The values are reported in Figure 3. The FEM appears to be more time consuming than the BEM when the same number of nodes is used. It is clear from the two curves in the figure that the CPU requirement tends to grow much faster for the FEM ($\approx N^{2.36}$) than for the BEM ($\approx N^{1.2}$). Although these comparisons appear to be conclusive, they should not be regarded as so. First, additional calculations must be carried out involving a geometry other than that of

a cube. The present cubic cavity represents the case typical of a bulky body where the ratio of volume-to-surface elements is of the same order in number. In this case, the BEM has the clear advantage over the FEM, given the relatively large number of volume elements involved. Cases involving thin cavities where the ratio of the number of volume-to-surface elements is small imply a relatively large number of boundary elements. In this case, the BEM loses some of its advantage over the FEM. Second, an accurate comparison and asymptotic

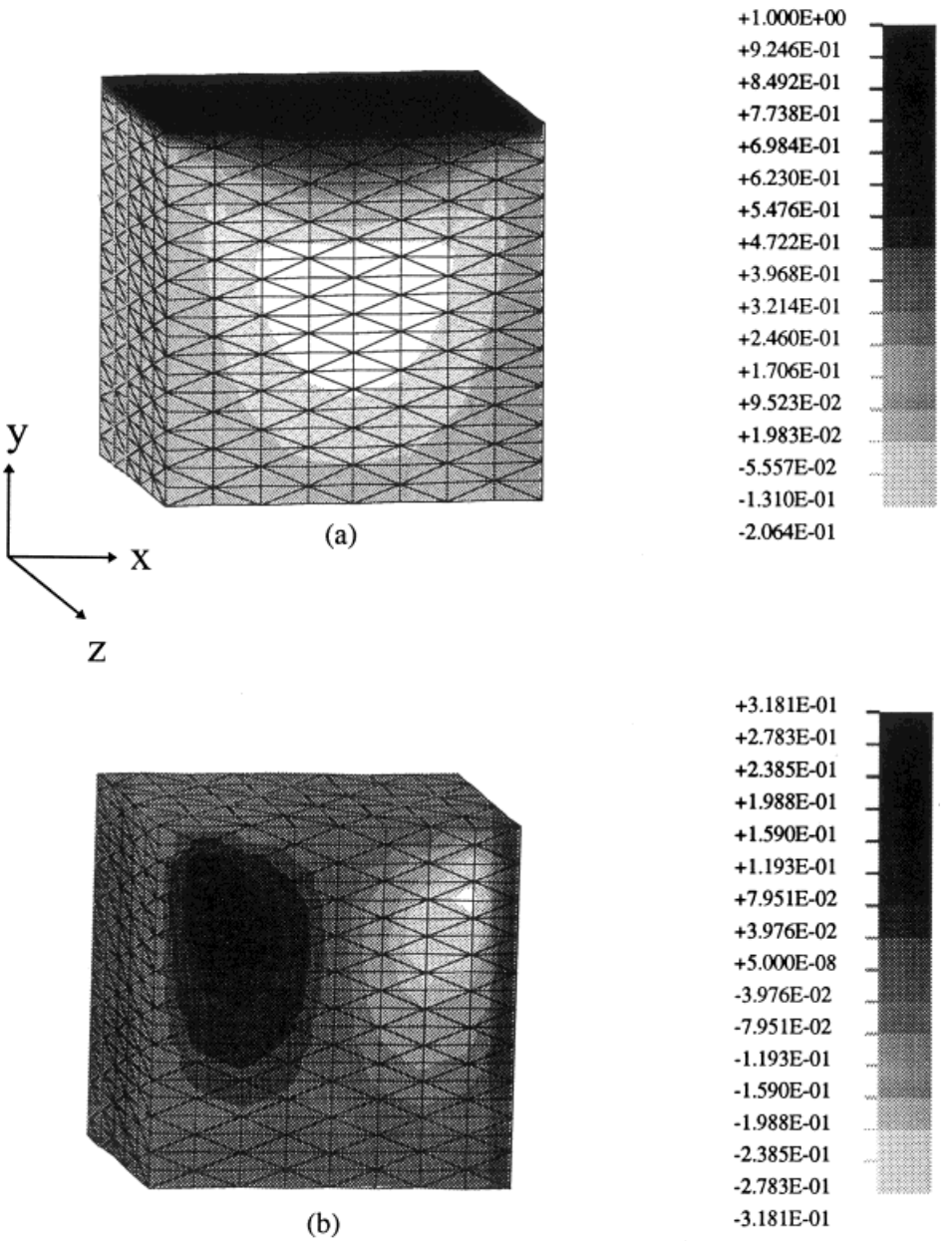

Figure 1. Flow of a Newtonian fluid inside a cubic cavity of unit dimension. Boundary element mesh, and u_x- and u_y-velocity contours in the lubricated plane $z = 1$ in (a) and (b), respectively.

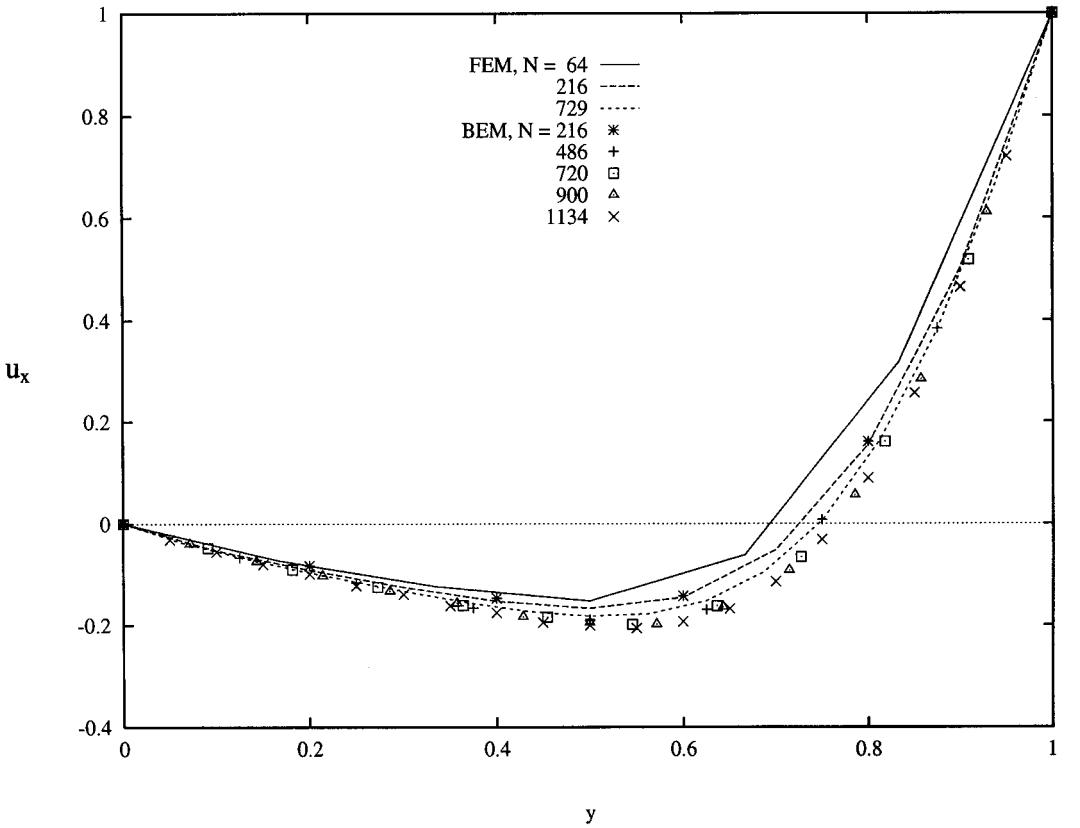

Figure 2. Comparison between the BEM and FEM for the cavity flow of a Newtonian fluid. Curves showing velocity distribution for $u = u_x$ along the y-axis at the center of the lubricated plane.

storage assessment between the two algorithms is difficult to achieve since the present BEM code and the POLYFLOW™ code may not be constructed in a similar manner. The main reliable information that one may retain from Figure 3 is the rate at which the CPU grows in each of the two cases.

4.2. Assessment of convergence and accuracy for viscoelastic fluids

The accuracy of the viscoelastic formulation is assessed through comparison with the analytical solution for a fluid placed between two concentric cylinders of infinite lengths. The outer-to-inner radius ratio is 2 and the inner cylinder is assumed to rotate at a dimensionless speed $V(t)$ with the outer cylinder remaining stationary. All variables are made dimensionless with respect to the inner cylinder radius, R_i (reference length), the ratio R_i/V_i (reference time) where V_i is a typical velocity of the inner cylinder, and $\mu V_i/R_i$ (reference stress). For the simulation, the height of the cylinders is taken equal to 1. Two different mesh sizes are considered, consisting of 312 and 1200 boundary elements. In order to reproduce the Taylor–Couette flow between two infinite cylinders, symmetry conditions are imposed on the top and bottom faces. Thus, the normal component of the velocity as well as the tangential stress components are taken equal to zero at the two faces. The inner cylinder is assumed to start rotating at constant speed π suddenly from rest, such that $V(t) = \pi H(t)$, where H is the

Heavyside function. Of particular interest is the evolution of the shear stress at the inner (or outer) cylinder. The corresponding analytical solution for the magnitude of the shear stress at the inner cylinder is equal to $4\pi/3\,(1-\mathrm{e}^{-t/\lambda})$. Note that λ is now dimensionless.

For the two mesh sizes reported, the shear stress at a given axial position (height) is found to be essentially constant along the circumferential direction (up to the fourth decimal). Figure 4 displays the distribution of the (steady) shear stress along the inner cylinder in the limit $t \to \infty$ for the viscoelastic fluid ($\lambda = 0.1$). This solution also corresponds to the Newtonian limit. The figure shows an improvement in the average error from 14 to 1% as the mesh is refined. The agreement between the numerical and analytical solutions generally worsens near the top and bottom faces. This is expected in the boundary element formulation as a singularity arises in the value of the tractions near a corner. The effect of this singularity is local, as depicted from the figure. In fact, for a finer mesh, the singularity is stronger but its effect becomes more localized with further mesh refinement.

The evolution of the average shear stress at the inner cylinder is displayed in Figure 5 for $\lambda = 0.1$ and 1.0. The average is taken over the height of the cylinder for 1200 boundary elements. The stress for a viscoelastic fluid, unlike the velocity, does not instantaneously reach the steady state (Newtonian) value. It undergoes a period of monotonic growth and tends asymptotically to the Newtonian limit. The numerical error tends to grow with time but reaches the level corresponding to the Newtonian limit ($\approx 1\%$).

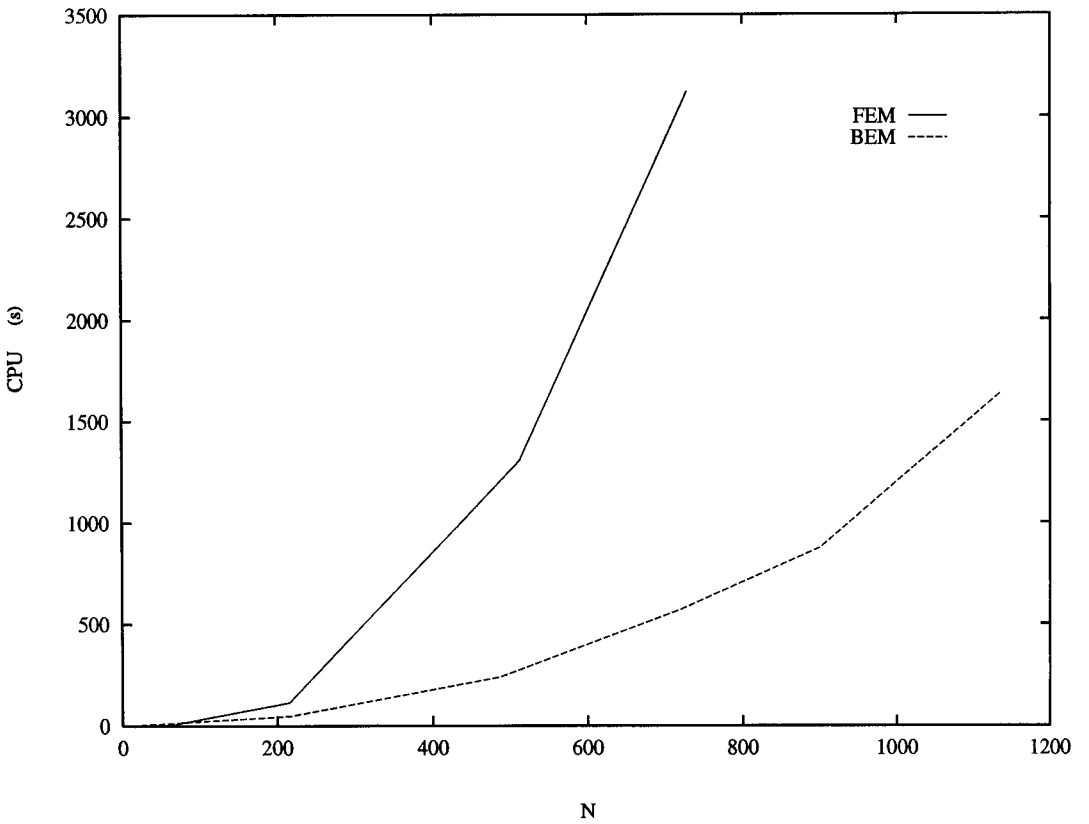

Figure 3. Comparison between the BEM and FEM for the cavity flow of a Newtonian fluid. Curves showing CPU requirement for both methods as function of number of total nodes used.

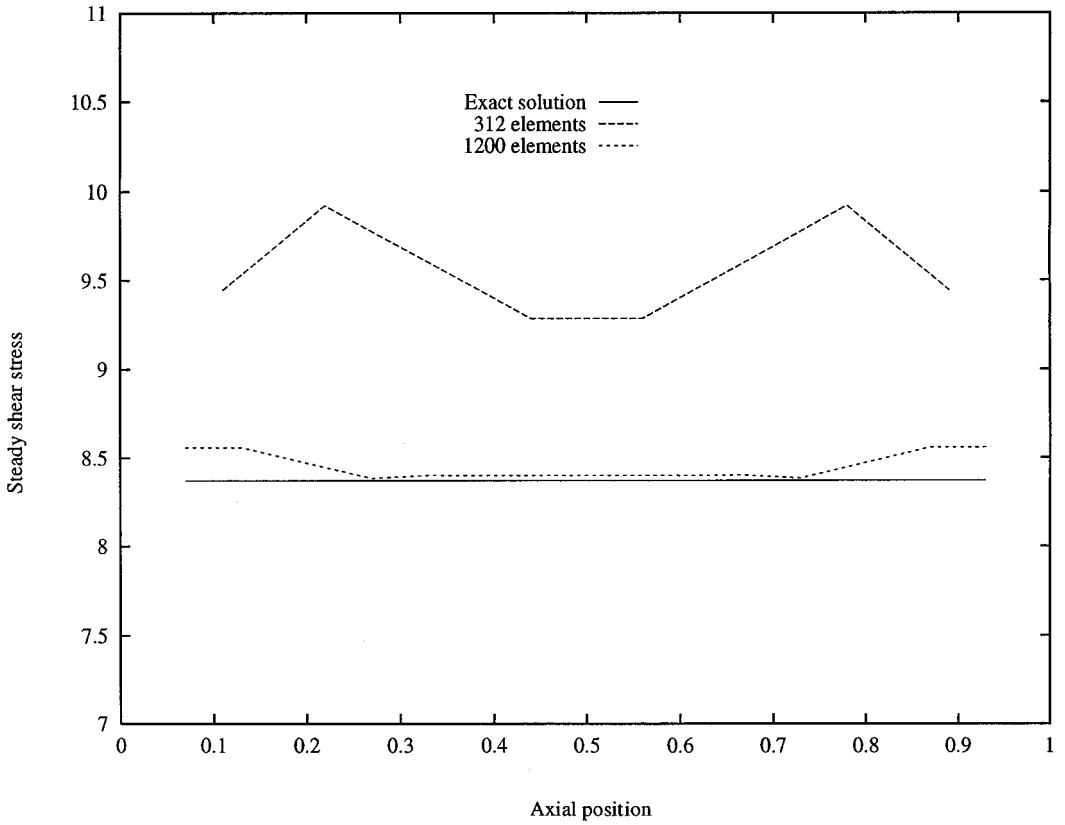

Figure 4. Comparison between the BEM and analytical results for the Taylor–Couette flow of Newtonian and viscoelastic fluids, and influence of mesh size. Steady shear stress distribution along the inner cylinder.

4.3. Comparison with experiment for a Newtonian fluid

Consider three cases of steady cavity flow as examined experimentally by Chien *et al.* [5] at low Reynolds number, *Re*. These are of the simple lid-driven cavity flow type where one or two faces move at a constant velocity. In the experiment, the flow was induced by the movement of elastic belts acting as moving walls. The Reynolds number in the experiment was of order one. This order of magnitude for *Re* was small enough for secondary flow and inertia effects to be avoided, but large enough to avoid the dye diffusion in the direction normal to the striations during the experiment in a given cavity. Although the present calculations are three-dimensional, special efforts were made in the experiment to produce two-dimensional flows. Possible variations of the velocity with the depth were checked by injecting a dye below the free surface of the transparent fluid used [5].

The three types of cavity flow used in experiments are conveniently referred to, as in Reference [5], as Type I cavity flow, for the standard cavity flow with one side moving; Type II, when two sides are moving in the same direction; and Type III, when two sides are moving in the opposite direction. In the present calculations, the cavity dimensions and belt velocity are taken exactly as in the experiment, although only the ratio of side lengths is of relevance, given the similarity in Stokes flow. In all three cases, stick conditions are applied on all sides except on the side where the flow was experimentally visualized (see also Figure 1 above). In

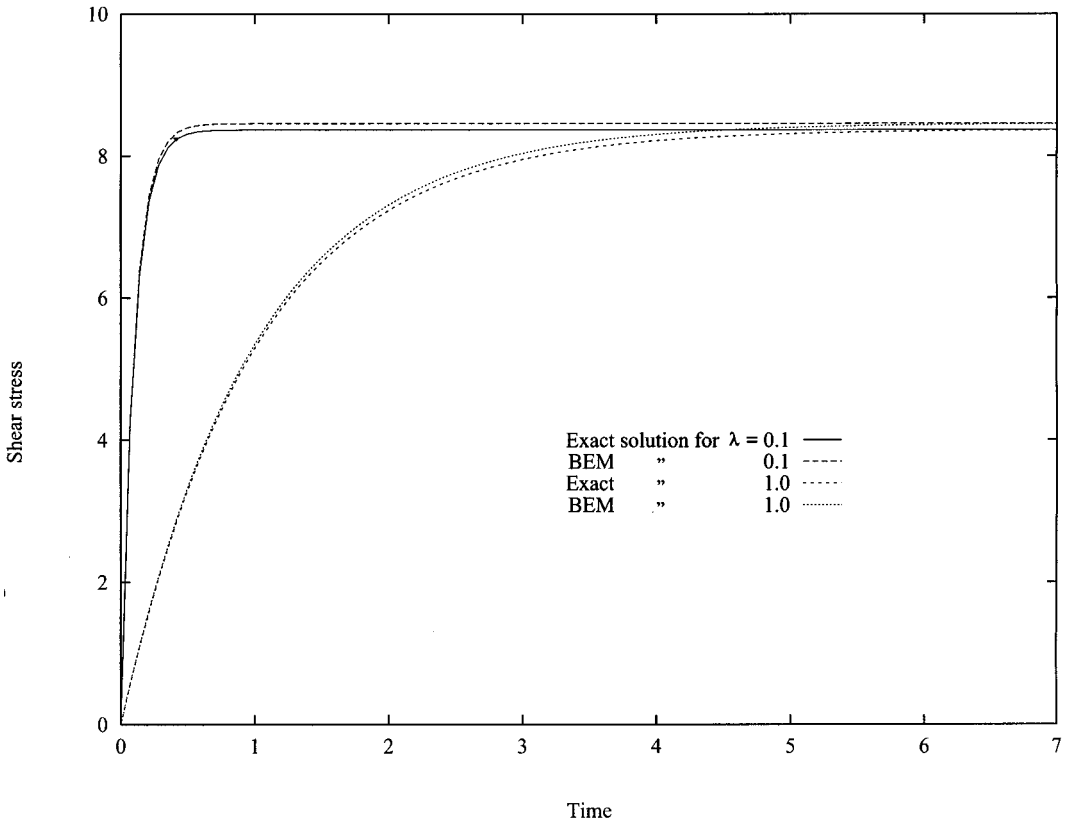

Figure 5. Comparison between the BEM and analytical results for the Taylor–Couette flow of viscoelastic fluids. Shear stress evolution with time for $\lambda = 0.1$ and 1.0 using 1200 boundary elements.

the figures below, the flow visualization reported by Chien *et al.* [5] is included for a comparison between theory and experiment. Note that no quantitative velocity profiles are available from the experiment that would allow a more direct comparison.

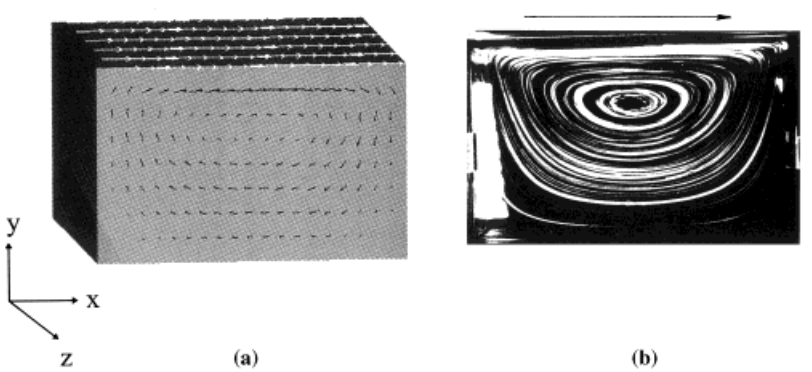

Figure 6. Comparison between theory and experiment for type I cavity flow of a Newtonian fluid. Computed flow based on the present BEM (a), and flow visualized from Chien *et al.*'s experiment [5] (b).

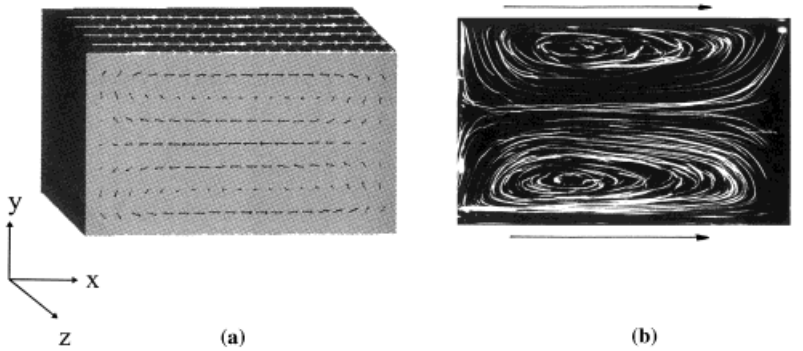

Figure 7. Comparison between theory and experiment for type II cavity flow of a Newtonian fluid. Computed flow based on the present BEM (a), and flow visualized from Chien *et al.*'s experiment [5] (b).

Consider the flow field for the three cavity types. The relative dimensions of each cavity are given by (11:6.5:5) in the (x, y, z) co-ordinates. Figure 6 shows the velocity field for Type I cavity flow based on the present formulation (Figure 6(a)) and that observed in the experiment (Figure 6(b)). Comparison between the two flows clearly indicates good agreement. The vortex center in the two cases is roughly located at the same relative position of 0.33 from the top side as measured from the experiment, and 0.31 from theory. Comparison is also satisfactory for Type II flow as shown in Figure 7. Note the slight shift to the right of the vortex center location. A similar conclusion is drawn for Type III flow from Figure 8. Chien *et al.* [5] reached a similar agreement between experiment and predictions based on their two-dimensional calculations carried out using the FEM of Malone [38]. The difference between two- and three-dimensional flows may be important depending on the influence of the edges of the cavity. This issue is next examined along with the (experimental) conditions under which the assumption of two-dimensionality may no longer be valid.

Calculations are carried out by varying the cavity depth for Type II flow. Two different rectangular shape cavities are used. The first, of dimensions 11:6.5:15, corresponds to that used in the experiment of Chien *et al.* [5], used also to compute the results reported in Figure 7. Additional calculations indicate that end effects tend to become significant only for a much shorter cavity. Thus, results based on the second geometry of dimensions 11:6.5:3.75 are presented. The corresponding flow configurations are shown in Figure 9. The flow in the plane

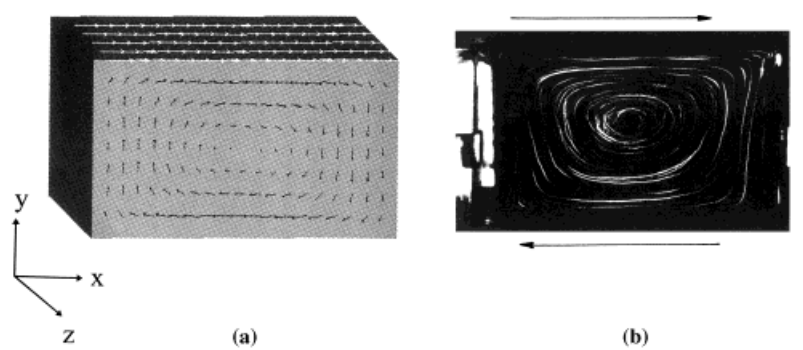

Figure 8. Comparison between theory and experiment for type III cavity flow of a Newtonian fluid. Computed flow based on the present BEM (a), and flow visualized from Chien *et al.*'s experiment [5] (b).

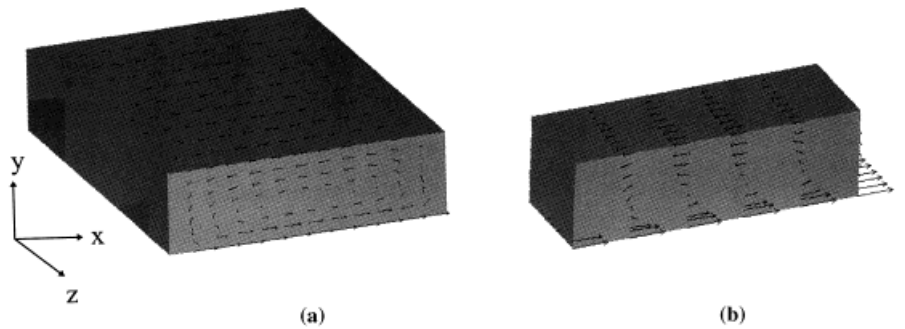

Figure 9. Edge effect in type II cavity flow. Negligible edge effects for long cavity (11:6.5:15) as shown in (a). Significant edge effects for short cavity (11:6.5:3.25) as shown in (b).

of symmetry is of particular interest here since this is where the influence of the edges will most likely show up. Indeed, Figure 9(a) shows, as expected, that end effects tend to be negligible given the large aspect ratio involved. This is obvious from the flow lines that reflect little change along the cavity depth. The flow corresponding to the shorter cavity is shown in Figure 9(b). In this case, the gradual increase in flow is evident in the vicinity of the back plane. The wall influence reaches roughly half way between the front and back planes. The flow in the front plane is essentially the same in both cases (both are outside the influence of the wall). This indicates that Chien *et al.* [5] could have used much shorter cavities and probably still ended up with essentially similar observations in their experiments.

4.4. Transient oscillatory flow of a Newtonian fluid

The implementation of the current method is illustrated for cavity flow of multiply-connected domains. Consider the flow inside a rectangular-shaped cavity, induced by the oscillatory motion of a smaller solid cube located inside the cavity. The outer cavity has relative dimensions 4:2:1 along the x-, y- and z-directions, while the inner (rectangular) solid has relative dimensions of 1:1:0.4, and is always constrained between the planes $z = 0.1$ and 0.5. Its center moves in the plane $y = 1.0$. The total number of boundary elements used in the simulation is equal to 1140. The results reported here are for three different positions of the inner solid as its center translates along the intersection between the planes $z = 0.3$ and $y = 1.0$. The fluid fills the region between the inner cavity walls and the outer surface of the solid obstacle, and is assumed to adhere to the solid cube while it slips along the inner walls of the rectangular-shaped cavity.

The results are shown in Figures 10–12 for three different positions of the inner solid center over one period of oscillation. Every point of the inner solid, located initially at x_0, is assumed to follow the trajectory $x(t) = x_0 + 1.5[1 - \cos(\frac{2}{3}t)]$, corresponding to a maximum dimensionless velocity equal to one when the solid is at the center of the cavity. The initial position of the inner solid is taken to be at the wall $x = 0$. Figure 10(a) shows the type and size of mesh used to discretize the surface of the cavity and that of the inner solid. The figure also shows that the inner solid is at a position close to the plane $x = 0$. In this case, the velocity is relatively small and the resulting flow is shown in Figure 10(b). The figure indicates, as expected, that most of the flow activity is concentrated near and in the plane $x = 0$. It is interesting to note that practically no flow takes place in almost half of the cavity. Note also the reduced flow activity in the planes other than $x = 0$, despite the fact that these planes are lubricated.

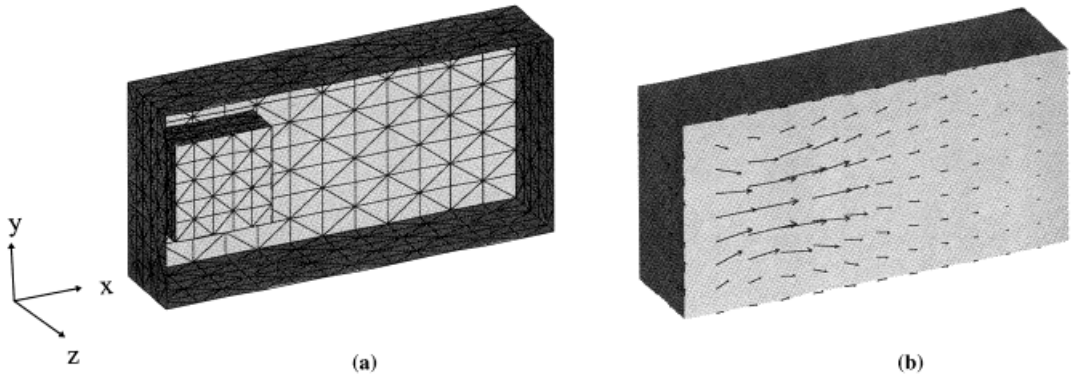

Figure 10. Oscillatory flow of a Newtonian fluid. Boundary element mesh and position of inner solid as the solid it accelerates from its initial position at $x = 0$ (a), and corresponding flow field (b).

When the inner solid reaches the center (Figure 11(a)) of the cavity, the velocity is at its highest value, and most of the flow activity is centered in the central region of the cavity as depicted from Figure 11(b). The situation in Figure 12 corresponds to the case when the inner solid is approaching the plane $x = 4$, after it has started to decelerate from the central region of the cavity. The flow in the reverse direction during the second half of the period is exactly symmetric to that shown in Figure 10. Note that, as an indication of the accuracy of the calculations, the flow is always symmetric with respect to the plane $y = 1.0$.

The present simulation illustrates the ability of the BEM to handle three-dimensional oscillatory flows. Other geometries than rectangular-shaped containers and cubic obstacles can easily be examined by the method. The implementation may be extended, for instance, to a cube rotating and oscillating at the same time. It is emphasized that complicated kinematics of the inner cube or other obstacles is not an issue for the BEM since the trajectory of each element that belongs to the obstacle boundary is in fact imposed. Although only the flow field in the (lubricated) plane of symmetry was of primary interest in the computation above, the BEM determines the distribution of traction, particularly the shear stress at sticky walls. The BEM also allows the visualization of the flow inside the cavity without extra (significant) cost. This is simply done by applying the first equation in (17) for a point belonging to the inside

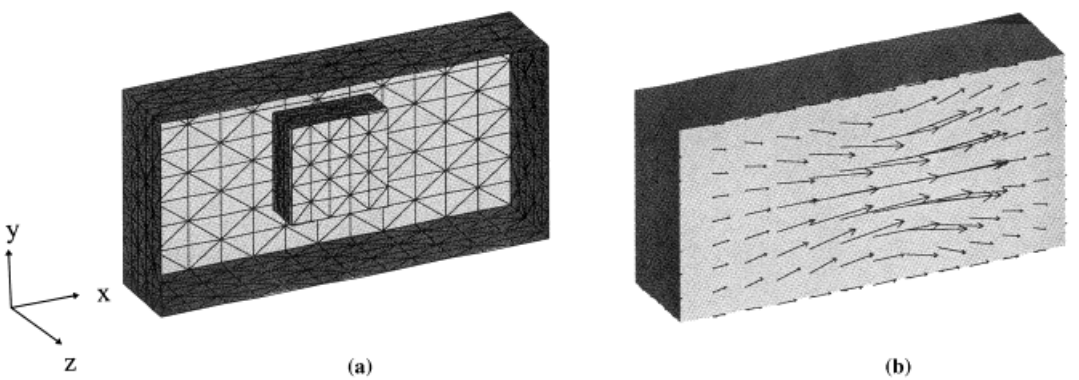

Figure 11. Oscillatory flow of a Newtonian fluid. Boundary element mesh and position of inner solid as the solid reaches the center of the rectangular shape cavity (a), and corresponding flow field (b).

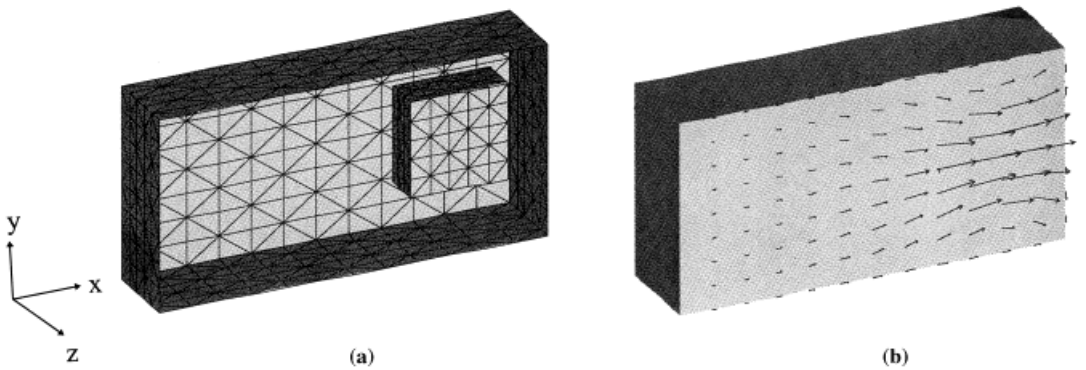

Figure 12. Oscillatory flow of a Newtonian fluid. Boundary element mesh and position of inner solid as the solid decelerates towards the plane $x = 4$ (a), and corresponding flow field (b).

of the domain of computation. The evaluation of the velocity at any internal point is determined through the evaluation of the surface integrals involving the flow field already determined from the solution of Equations (18) and (19).

4.5. Transient rotating flow of a Newtonian fluid

Consider now another category of transient flow motion as applied to mixing, namely the case of rotating flow in a rectangular-shaped cavity. The motion is induced by the action of a four-blade rotor, typically as it arises in mixing machines. The geometry and boundary element mesh, as well as the resulting flow, are shown in Figure 13. The outer cavity has a square base in the (x, y) plane with a side twice as long as the height. Although the dimensions of the rotor are not crucial in the present illustration, they can still be inferred from Figure 13(a). More importantly, it is the complexity of shape and the simplicity of the implementation of the BEM that are emphasized here. The total number of boundary elements is equal to 1460. As in the case of the previous (oscillatory) flow, the fluid is assumed to adhere to the rotor surface.

Some of the elements in the mesh shown in Figure 13(a) may look too distorted because of the three-dimensional perspective. Some level of distortion is in fact present in the elements, particularly those belonging to the rotor surface. Unlike the FEM, the BEM is capable of

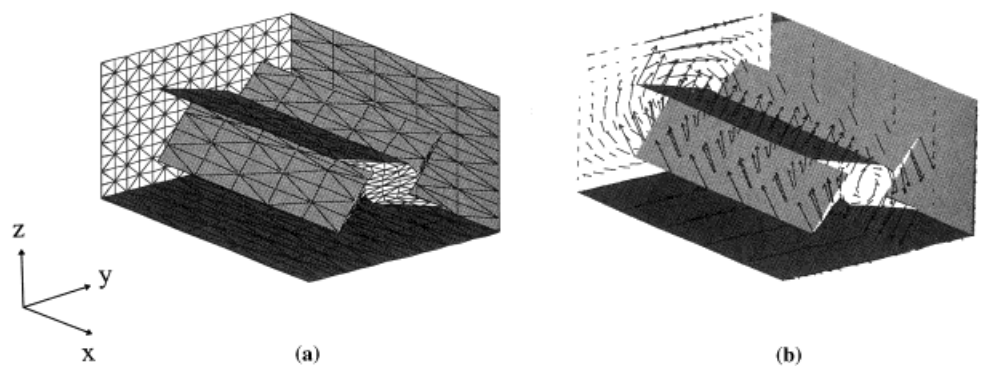

Figure 13. Rotating flow of a Newtonian fluid. Boundary element mesh (a) and flow field (b). Adherence is assumed on the rotor walls, while the inner cavity walls are assumed to be lubricated.

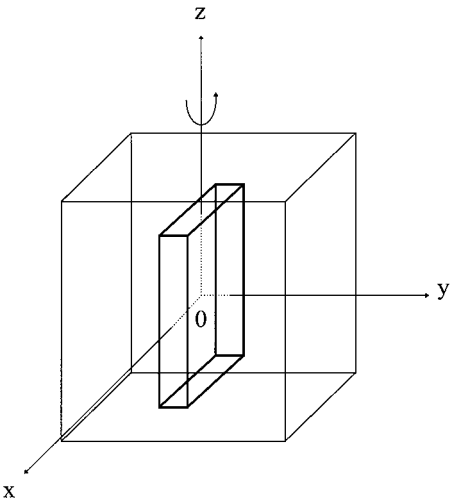

Figure 14. Rotating vane in a cubic cavity. Figure illustrates relative dimensions and initial position of the vane.

more efficient handling of element distortion given the denseness of the matrix corresponding to the final algebraic system. Note that there is a clearance between the ends of the rotor and the lateral walls of the cavity. The resulting flow field shown in Figure 13(b) corresponds to a rotor rotating clockwise. In order to aid visualization, the inner walls of the cavity are assumed lubricated. In this case, the fluid flows on the cavity walls as illustrated in Figure 13(b). Several additional aspects can be explored in the context of mixing using the present formulation, but are not examined here in order to remain within the preliminary nature of the present study.

For instance, other more realistic (rotor and cavity) geometries, as well as different boundary conditions, are possible to handle without additional computational effort, except that the meshing stage will likely be more involved for a more complex geometry (such as the case of a screw mixer). Stick boundary conditions are easily imposed on the inner cavity walls. In this case, although no flow takes place at the cavity walls, the torque may be determined from the traction distribution at both the rotor and the cavity walls. It is emphasized at this stage, that the inner flow field is also easily obtainable after the boundary variables are determined. The inner flow field is important for problems in mixing since the relatively active and stagnant flow regions can be identified.

4.6. Transient rotating flow of a viscoelastic fluid: non-linear dynamics

The investigation of rotating mixing flow is pursued further by examining the effect of viscoelasticity. Given the large number of time steps involved in the calculations, the investigation is limited to a simpler configuration than that shown in Figure 13. So, consider the three-dimensional cavity flow inside a cube of dimensions: $-0.5 \le x \le 0.5$, $-0.5 \le y \le 0.5$, $-0.5 \le z \le 0.5$, with the origin coinciding with the center of the cube. The flow is induced by the rotation of a flat rectangular rotor (vane) initially occupying the region $-0.1 \le x \le 0.1$, $-0.4 \le y \le 0.4$, $-0.4 \le z \le 0.4$ as illustrated in Figure 14. At $t = 0$, the rotor is set in counter-clockwise motion (around the vertical y-axis) at an angular speed of one revolution per unit time. Since the fluid responds immediately to the motion of the rotor, the flow field is the same for both Newtonian and (linear) viscoelastic fluids. For this reason, viscoelasticity only influences the evolution of stress or traction at the rotor and inner cavity walls, which will now be examined under conditions of complete stick at the boundaries.

The evolution of the traction at the rotor tip, at the point located initially at (0.0, 0.0, 0.4), is monitored over a period of two revolutions. Both Newtonian fluids ($\lambda = 0$) and viscoelastic fluids with $\lambda = 0.1$, 0.2 and 0.3 are examined. The evolutions of the traction components t_x and t_z are shown in Figures 15 and 16, respectively. For a Newtonian fluid, in contrast to viscoelastic fluids, there is a small but non-zero t_x value at $t = 0$ (Figure 15) equal (in magnitude) to the slope $u_{x,z}(0.0, 0.0, 0.4)$. The periodic behavior in t_x is clearly depicted from Figure 15. For $\lambda > 0$, t_x increases from zero, and eventually settles in turn into a similar periodic signal with the same frequency as the Newtonian signal. There is a phase shift relative to the Newtonian signal that increases as the level of fluid elasticity increases. The amplitude of the stress decreases as the fluid becomes more elastic. The figure also shows that any modulation or non-linear behavior in the time signature tends to disappear as λ increases.

The evolution of t_z at the same location is shown in Figure 16. In this case, the difference in initial behavior between Newtonian and viscoelastic flows is more obvious. This difference is most probably due to the effect of the (hydrostatic) pressure since $u_{z,z}$ is not expected to be large compared with $u_{x,z}$ at (0.0, 0.0, 0.4) over a 0.1 gap between the tip of the rotor (at the plane $z = 0.4$) and the opposite cavity side ($z = 0.5$). The component t_z increases monotonically with time for viscoelastic fluid until periodic behavior is attained.

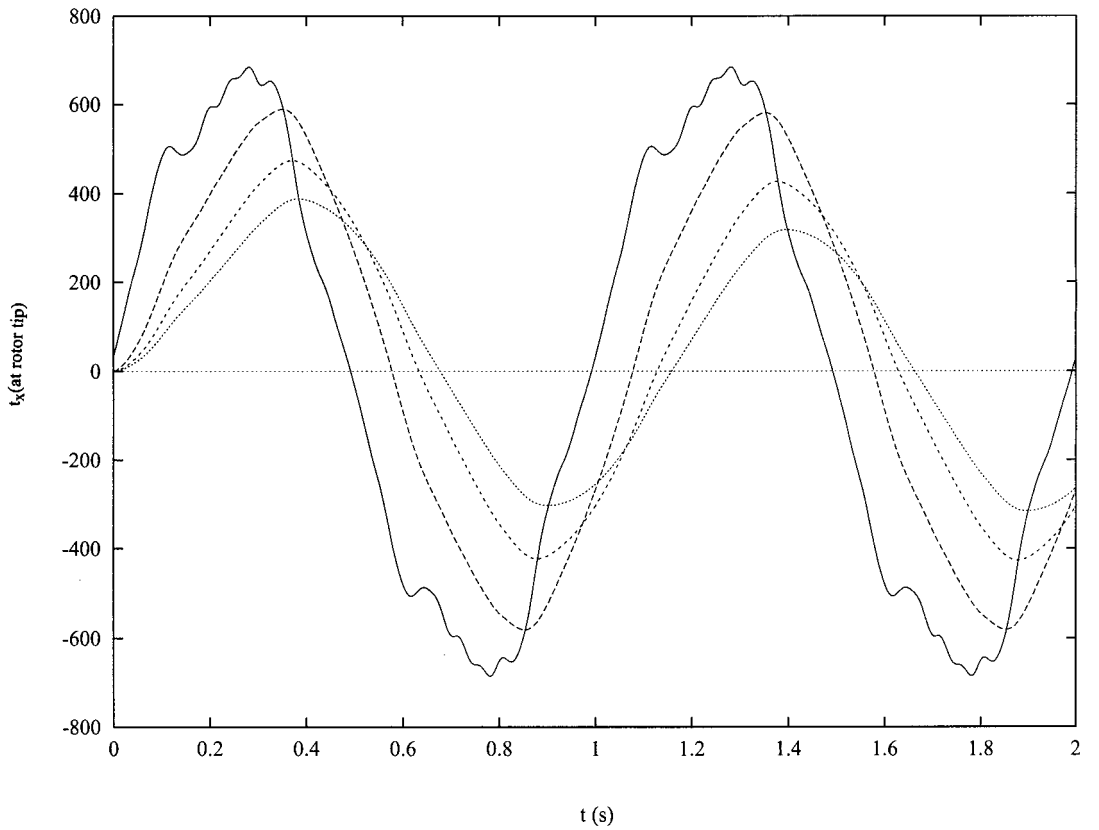

Figure 15. Evolution of t_x at the tip of the rotor, at the point initially located at (0.0, 0.0, 0.4). The long-term signal period is 1 s, corresponding to a full revolution of the rotor. Newtonian fluid (—), viscoelastic fluid with $\lambda = 0.1$ (- - - -), 0.2 (– – – –) and 0.3 (···).

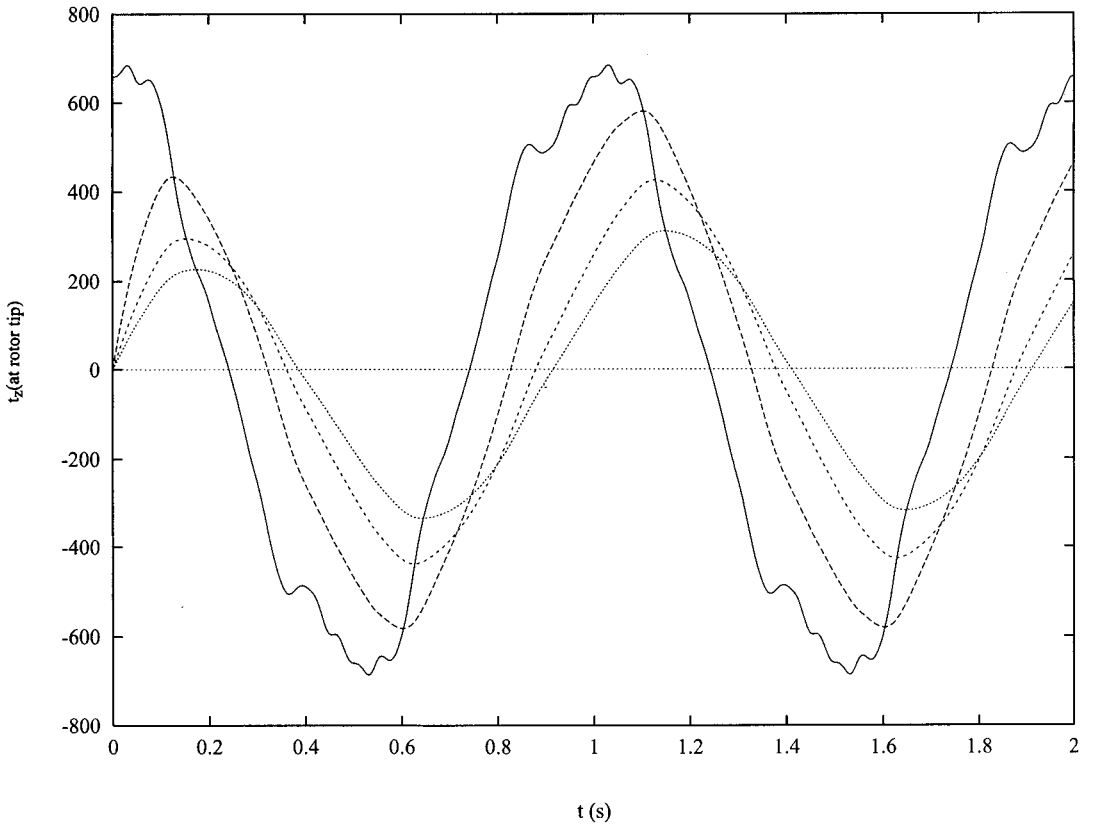

Figure 16. Evolution of t_z at the tip of the rotor, at the point initially located at (0.0, 0.0, 0.4). The long-term signal period is 1 s corresponding to a full revolution of the rotor. Newtonian fluid (—), viscoelastic fluid with $\lambda = 0.1$ (- - - -), 0.2 (– – – –) and 0.3 (···).

5. DISCUSSION AND CONCLUSION

In this study, the applicability of the BEM to problems of relevance to the mixing processes is demonstrated for Newtonian and viscoelastic fluids. These processes are typically unsteady and involve the presence of at least one moving boundary, that of a rotor or stirrer. The performance of the BEM is assessed against that of the FEM (using POLYFLOW™) for a simple lid-driven cavity flow of a Newtonian fluid. The BEM appears to require less CPU than the FEM for a mesh involving the same number of nodes (internal and external). A direct quantitative comparison is difficult to attain, however, given that the two numerical algorithms are designed differently. What is more conclusive is the rate at which CPU requirement increases with the number of nodes. The rate is much larger in the case of the FEM than that of the BEM.

Since the emphasis of the study is on the potential applicability of the BEM to problems in polymer processing, many relevant numerical issues are not fully covered. The study is not intended to deal with complex numerical issues of the BEM. It is rather aimed at demonstrating the simplicity of the BEM as it is applied to complex three-dimensional flow, with emphasis on mixing. The discretization of the boundary is carried out using constant elements. Although considerable progress has been made since the earlier implementation of constant BEM, much

of this progress was destined to two-dimensional problems. Ultimately, the choice of constant or higher-order elements is influenced by the degree of accuracy desired versus the algorithmic complexity in implementation, and the subsequent requirement for storage and CPU. The problem of evaluating singular integrals is just one of the major difficulties facing the use of higher-order elements. The present study explores the applicability of the BEM in areas of polymer processing where conventional volume methods are difficult to implement. The complexity of the various problems examined here must not be underestimated. The suitability of the BEM, its relatively high accuracy, and the simplicity in implementation (especially when constant elements are used) are clearly illustrated throughout the work.

The use of constant elements greatly simplifies the implementation for complex flows. Traction multiple-valuedness is probably the most crucial issue when dealing with higher-order BEM for a complex geometry. For constant elements, the traction is determined (or imposed) at the centroid of the element. It is thus uniquely defined. When higher-order elements are used, the traction is determined as a nodal variable on the discretized boundary. In this case, the traction is generally not single-valued since the normal at a node is not uniquely defined.

In two-dimensional flow, the problem is easily circumvented since a node always belongs to two segments of the boundary. The traction is thus at most, double-valued for a general discretized (curved) boundary. Two methods are used for planar flow; the discussion is limited to linear elements. The first method consists of computing the two discontinuous values of the traction vector at each node where the traction is unknown, and one value of the continuous velocity where the velocity is to be determined. The second method consists of shifting the two nodes of each connecting segment some distance apart. There is thus no node at the intersection between two consecutive segments and therefore no discontinuity in traction. The situation is much more complicated for three-dimensional flow [43,44,47].

For three-dimensional boundary domains, the traction can be multiple-valued since a node may belong to several elements. The number of connecting elements can be arbitrary and may vary from one node to the next. The number of unknown tractions varies accordingly. The methods described above that are easily implementable in the plane become inapplicable for three-dimensional flow. Only in simple three-dimensional geometry, involving intersecting planar surfaces, that the issue of traction multiple-valuedness can be handled without major difficulty. In the case of a rectangular-shaped cavity, for instance, the traction is single-valued except at a corner node where it is triple-valued, since a corner node belongs to three planes. Trang-Cong and Phan-Thien examined a similar problem for the flow at the exit of a square tube [39]. According to the case studies examined in the present work, higher-order elements could be used since the geometry is only moderately complex. The number of intersecting planes for each corner node is clear and the planes are easily identifiable. For a general surface (such as moving interfaces or free surfaces), however, there is no systematic way of approaching the problem of multiple-valued traction.

Another aspect of constant elements is the emergence of a singularity in the traction at a corner. This is a problem that does not arise when higher-order elements are used. However, corner singularities are well-known for Stokes flow. The singularities are related to the breakdown in similarity solutions. The problems of pressure-driven flow along a duct whose cross-section has a sharp corner [40], the planar flow near a corner in a right-angle wedge [41], or, more generally, flows that contain eddies or closed streamlines [42] are typical situations with corner singularities. In BEM calculations, the singularity in traction at a

corner appears to be a local phenomenon; the flow field far from the corner is not influenced by the singularity. More generally, mesh refinement leads to more local but stronger singularity. The localized effect is clearly illustrated in Figure 4. Corner singularities are present in all the case studies examined in the present study. However, there is no loss of accuracy resulting from using constant elements. The comparative calculations against the FEM (Figures 2 and 3), against analytical solution (Figures 4 and 5) for Newtonian and viscoelastic fluids, and against experiment for lid-driven flows (Figures 6–8) clearly demonstrate the validity of the formulation. Excellent agreement between constant element BEM and FEM results was also achieved in a previous study [14].

The viscoelastic formulation is validated against the analytical solution for sudden inception Taylor–Couette flow. The BEM code is further validated upon comparison with the experiment of Chien *et al.* [5] for lid-driven cavity flows. There is generally good agreement between the simulation and the flow visualized in the experiment. Since long cavities were used in the experiment, the flow was essentially two-dimensional. In order to assess the influence of the cavity edges, additional calculations are carried out by varying the length of the cavity. It is found that three-dimensional effects become significant only for very short cavities.

Newtonian and viscoelastic flow problems involving more complex three-dimensional geometry and transient behavior, typically as they arise in polymer mixing processes are examined. The resulting computational domain is multiply-connected given the presence of the moving obstacle (stirrer) inside the cavity. In this case, the BEM is particularly convenient to implement since, unlike conventional numerical methods, it does not require the discretization of the inner (volume) domain that is bounded by the stirrer outer surface and the inner walls of the cavity.

The oscillatory and rotating flows for a Newtonian fluid are investigated, and are induced by the action, respectively, of a solid cube and a rotor inside rectangular cavities. The influence of viscoelasticity is clearly illustrated in the case of rotating flow inside a cubic cavity with sudden inception in the motion of the rotor. The evolution of the tractions at the rotor tip reveals complex dynamics and transient behavior. While the traction for a Newtonian fluid settles into periodic motion right from the beginning, the traction for a viscoelastic fluid is found to undergo a transient evolution before it reaches periodic behavior. The viscoelastic signal generally exhibits a phase shift and has an amplitude that decreases as the level of fluid elasticity increases. While the constitutive equations used (for creeping Newtonian and Maxwell fluids) are linear, the response of the traction is highly non-linear.

Some immediate extensions of the present formulation may be mentioned. The method is capable of handling more complex geometries for both the container (cavity) and the solid body (stirrer) moving inside, or the case of an obstacle (stirrer) undergoing simultaneous translation and rotation. Single- and twin-screw mixers are typical examples. Another extension involves the free motion of a solid body inside a cavity (of the lid-driven type). In this case, the kinematics of the nodes or boundary elements on the surface of the body are no longer imposed, and thus must be determined as part of the solution. This, by itself, does not pose any serious difficulty; additional complications may arise when the (freely) moving body comes in contact with the walls of the cavity. Some care must then be taken in choosing the type of boundary conditions to be imposed in this case.

REFERENCES

1. G. de Vahl Davis and G.D. Mallison, 'An evaluation of upwind and central difference approximation by a study of recirculating flow', *Comput. Fluids*, **4**, 29 (1976).
2. R. Pan and A. Acrivos, 'Steady flows in rectangular cavities', *J. Fluid Mech.*, **28**, 643 (1967).
3. R. Schreiber and H.B. Keller, 'Spurious solutions in a driven cavity calculations', *J. Comp. Phys.*, **49**, 165 (1983).
4. R. Peyret and T.D. Taylor, *Computational Methods of Fluid Flow*, Springer, Berlin, 1983.
5. W.L. Chien, H. Rising and J.M. Ottino, 'Laminar mixing and chaotic mixing in several cavity flows', *J. Fluid Mech.*, **170**, 355 (1986).
6. S. Smale, 'Differentiable dynamical systems', *Bull. Am. Math. Soc.*, **73**, 747 (1967).
7. C.W. Leong and J.M. Ottino, 'Experiments on mixing due to chaotic advection in a cavity', *J. Fluid Mech.*, **209**, 463 (1989).
8. A.B. Cortes and J.D. Miller, 'Numerical experiments with the lid-driven cavity flow problem', *Comput. Fluids.*, **23**, 1005 (1994).
9. P.J. Gramann, L. Stradins and T.A. Osswald, 'Flow and heat transfer simulation of the mixing of polymer blends using the boundary element method', *Int. Polym. Process.*, **8**, 287 (1993).
10. K. Gustafson and K. Halasi, 'Vortex dynamics of cavity flows', *J. Comp. Phys.*, **64**, 279 (1986).
11. C.H. Bruneau and C. Jouron, 'An efficient scheme for solving steady incompressible Navier–Stokes equations', *J. Comp. Phys.*, **89**, 389 (1990).
12. J.W. Goodrich, K. Gustafson and K. Halasi, 'Hopf bifurcation in the driven cavity', *J. Comp. Phys.*, **90**, 219 (1990).
13. J. Shen, 'Hopf bifurcation of the unsteady regularized-driven cavity flow', *J. Comp. Phys.*, **95**, 228 (1991).
14. R.E. Khayat, A. Derdouri and L.P. Hebert, 'A three-dimensional boundary element approach to gas-assisted injection moulding', *J. Non-Newt. Fluid Mech.*, **57**, 253 (1995).
15. D. Frayce, R.E. Khayat and A. Derdouri, 'A dual reciprocity approach to three-dimensional transient heat conduction as applied to materials processing', *J. Numer. Heat Transf. A*, **29**, 243 (1996).
16. R.E. Khayat and D. Frayce, 'Simulation of transient 3D free surface flow in a shot sleeve of die casting machines', in P.E. Raad, T.T. Huang and G. Tryggvason (eds), *Advances in Numerical Modeling of Free Surface and Interface Fluid Dynamics*, FED 234, ASME, New York, 1995, p. 207.
17. R.E. Khayat, A. Luciani and L.A. Ukacki, 'Boundary element analysis of planar drop deformation in confined flow. Part i. Newtonian fluids', *Eng. Anal. Bound. Elem.*, **19**, 279 (1997).
18. T. Tran-Cong and N. Phan-Thien, 'Three-dimensional study of extrusion processes by boundary element method. II. Extrusion of a viscoelastic fluid', *Rheol. Acta*, **27**, 639 (1988).
19. R.I. Tanner, *Engineering Rheology*, Clarendon Press, Oxford, 1985.
20. P.W. Partridge, C.A. Brebbia and L.C. Wrobel, *The Dual Reciprocity Boundary Element Method*, Computational Mechanics Publications, Southampton, 1992.
21. A.J. Nowak, 'Application of the multiple reciprocity method for solving nonlinear problems', in L.C. Wrobel, C.A. Brebbia and A.J. Nowak (eds), *Advanced Computational Methods in Heat Transfer II, vol I: Conduction, Radiation and Phase Change*, Computational Mechanics Publications, Southampton, 1995.
22. A.C. Neves and C.A. Brebbia, 'The multiple reciprocity boundary element method for transforming domain integrals to the boundary', *Int. j. numer. methods eng.*, **31**, 709 (1991).
23. F.J. Rizzo and D.J. Shippy, 'An application of the corresponding principle of viscoelastic theory', *SIAM J. Appl. Math.*, **21**, 321 (1971).
24. T. Kusama and Y. Mitsui, 'Boundary element method applied to linear viscoelastic analysis', *Appl. Math. Model.*, **6**, 285 (1982).
25. R.M. Christensen, *Theory of Viscoelasticity*, 2nd edn, Pergamon, Oxford, 1982.
26. D.R. Bland, *Theory of Linear Viscoelasticity*, Pergamon, Oxford, 1960.
27. B. Gross, *Mathematical Structure of the Theory of Viscoelasticity*, Hermann, Paris, 1968.
28. W.T. Read, 'Stress analysis for compressible viscoelastic materials', *J. Appl. Phys.*, **21**, 671 (1950).
29. R. Sips, 'General theory of deformation of viscoelastic substances', *J. Ploym Sci.*, **9**, 191 (1951).
30. M.A. Brull, 'A structural theory incorporating the effect of time-dependent elasticity', *Proc. 1st Midwestern Conf. Solid Mechanics*, 1953, p. 141.
31. E.H. Lee, 'Stress analysis in viscoelastic bodies', *Quart. Appl. Math.*, **13**, 183 (1955).
32. C. Pozrikidis, *Boundary Integral and Singularity Methods for Linearized Viscous Flow*, Cambridge University Press, Cambridge, 1992.
33. O.A. Ladyzhenskaya, *The Mathematical Theory of Viscous Incompressible Flow*, Gordon and Breach, New York, 1969.
34. M.J. Martinez and K.S. Udell, 'Axisymmetric creeping motion of drops through circular tubes', *J. Fluid Mech.*, **210**, 565 (1990).
35. J.M. Rallison and A. Acrivos, 'A numerical study of the deformation and burst of a viscous drop in an extensional flow', *J. Fluid Mech.*, **89**, 191 (1978).
36. X.Z. Li, D. Barthes-Riesel and A. Helmy, 'Large deformation and burst of a capsule freely suspended in an elongational flow', *J. Fluid Mech.*, **187**, 179 (1988).
37. T.A. Cruse, 'Numerical simulation in three-dimensional elastostatics', *Int. J. Solids Struct.*, **5**, 1259 (1969).

38. M.F. Malone, 'Numerical simulation of hydrodynamics problems in polymer processing', *Ph.D. Thesis*, University of Massachusetts, Amherst, MA, 1985.
39. T. Tran-Cong and N. Phan-Thien, 'Three-dimensional study of extrusion processes by boundary element method. I. An implementation of high-order elements and some Newtonian results', *Rheol. Acta*, **27**, 21 (1988).
40. H.K. Moffatt and B.R. Duffy, 'Local similarity solutions and their limitations', *J. Fluid Mech.*, **96**, 299 (1980).
41. T.S. Krasnopolskaya, 'Two-dimensional Stokes flow near a corner in a right angle wedge and Moffatt's eddies', *Mech. Res. Comm.*, **22**, 9 (1995).
42. D.J. Jeffrey and J.D. Sherwood, 'Streamline patterns and eddies in low-Reynolds number flow', *J. Fluid Mech.*, **96**, 315 (1980).
43. C.A. Brebbia and J. Domingez, *Boundary Element: An Introductory Course*, Computational Mechanic Publications, Southampton, 1992.
44. M.B. Bush and N. Phan-Thien, 'Three dimensional viscous flows with a free surface: flow out of a long square die', *J. Non-Newt. Fluid Mech.*, **18**, 211 (1985).
45. C.J. Coleman, 'On the use of boundary integral methods in the analysis of non-Newtonian fluid flow', *J. Non-Newt. Fluid Mech.*, **16**, 347 (1984).
46. M.B. Bush, R.I. Tanner and N. Phan-Thien, 'A boundary element investigation of extrudate swell', *J. Non-Newt. Fluid Mech.*, **18**, 143 (1985).
47. P.K. Kythe, *An Introduction to Boundary Element Methods*, CRC Press, Boca Raton, 1995.
48. R.B. Bird, R.C. Armstrong, and O. Hassager, *Dynamics of Polymeric Liquids*, *vol. 1*, Wiley, New York, 1987.

